Optica Applicata, Vol. LV, No. 2, 2025
DOI: 10.37190/oa/195795

Design of high precision microscope objective for optical-fiber-fusion-splicing based on apochromatic theory

XINGYUN ZHANG[1,2,3], YANHONG GAO[4], YIQUN JI[1,2,3,*], SHIJIA ZHAO[1,2,3]

[1]Soochow University, School of Optoelectronic Science and Engineering, Suzhou, 215006, China

[2]Soochow University, Collaborative Innovation Center of Suzhou Nano Science and Technology & Engineering Research Center of Digital Imaging and Display of Education Ministry of China, Suzhou, 215006, China

[3]Soochow University, Key Lab of Advanced Optical Manufacturing Technologies of Jiangsu Province & Key Lab of Modern Optical Technologies of Education Ministry of China, 215006, China

[4]Suzhou City University, School of Optical and Electronic Information, Suzhou, 215006, China

[*]Corresponding author: jiyiqun@suda.edu.cn

With the rapid development of optical fiber communication technology, the requirement for high -quality splicing has also increased. The accuracy of optical fiber alignment is the most crucial factor in determining splicing quality. The imaging quality of the microscope objective and the accuracy of the optical fiber alignment algorithm together determine the accuracy of optical fiber alignment. This paper proposes a new alignment method based on the black line at the interface between optical fiber core and cladding. The imaging characteristics of the black line are analyzed, and the initial structure of the microscope objective is deduced based on the theory of apochromatism, and finally a high-precision optical fiber fusion splicing microscope objective with a waveband from 460 to 660 nm is designed. An experimental device is set up to obtain optical fiber images, and the results indicate that the microscope objective plays a significant role in magnifying black lines. The horizontal and vertical offsets of optical fiber can be accurately identified through image processing. This paper considers the lens design theory and feature recognition algorithm comprehensively to improve the accuracy of optical fiber alignment, ultimately achieving high-quality optical fiber fusion splicing.

Keywords: optical-fiber-fusion-splicing, microscopic imaging, optical design, imaging processing.

1. Introduction

The 21st century is the age of information. With the rapid development of information technology, as the foundation of modern communication, optical fiber communication has received extensive attention [1]. However, due to production constraints, the standard length of the cable is usually only 1–2 km [2]. Therefore, a significant amount of

fiber splicing work is required. The transmission capacity of the optical fiber is determined by the loss generated during the splicing process [3,4]. Although the loss of the optical fiber itself is inevitable during the optical cable construction process, the loss at the joint can be reduced through technical means. Fiber to the home (FTTH) has been a research hotspot in optical fiber communication in recent years. Therefore, the development of fiber splicing technology is imperative and has broad application prospects. Optical fiber is a transmission medium made of quartz material. Its size ranges from a few microns to a few hundred microns. Optical fiber fusion splicer is capable of performing high-volume fiber fusion splicing, effectively solving the problem of inaccurate fusion splicing that cannot be achieved manually, as well as high fusion splice loss [5]. As an important equipment in the field of optical fiber communication, the development direction of optical fiber fusion splicer is mainly focused on intelligence and miniaturization, with the goal of improving the quality and speed of fusion splicing. The application of intelligent technology can effectively reduce the uncertainty of manual operation, enhance the stability and consistency of fusion splicing, ultimately improving the overall quality of the process [6,7]. The miniaturized design of the optical fiber fusion splicer allows for greater adaptability to special environments, such as narrow construction spaces or poor construction conditions [8].

In summary, in order to further enhance the construction and maintenance efficiency of optical fiber communication networks and promote the rapid development of optical fiber communication technology, optical fiber fusion splicers are developing in the direction of intelligence and miniaturization. With the continuous innovation of technology and the continuous growth of market demand, the requirements for the fusion splicing quality of optical fiber fusion splicer are also increasing, and the most important factor in determining the quality of fusion splicing is the precision of optical fiber alignment, so the study of high precision optical fiber fusion splicing microscope objective is of great significance.

2. Analytical design

Due to the different refractive indexes of the core and cladding in the fiber [9], the incident light is refracted when it is incident on the fiber from the side, creating a brightness distribution of light and dark, as shown in Fig. 1. By examining the emitted light, it can be seen that the light is deflected at the interface between the cladding and core. The refractive index of the fiber core is larger, and the light passing through the fiber core is more concentrated, while the convergence ability of the cladding is weaker. Therefore, a distinct black line is generated at the exit surface, which can be used as the basis for fiber splicing. The position of the fiber can be positioned more accurately, which reduces the design cost of the microscope objective accordingly.

As shown in Fig. 1, the propagation of parallel light into a fiber can be divided into two cases. In one case, the light enters the fiber and propagates only in the cladding. In the other case, the light propagates through the cladding, enters the core, exits the core, and enters the cladding again.

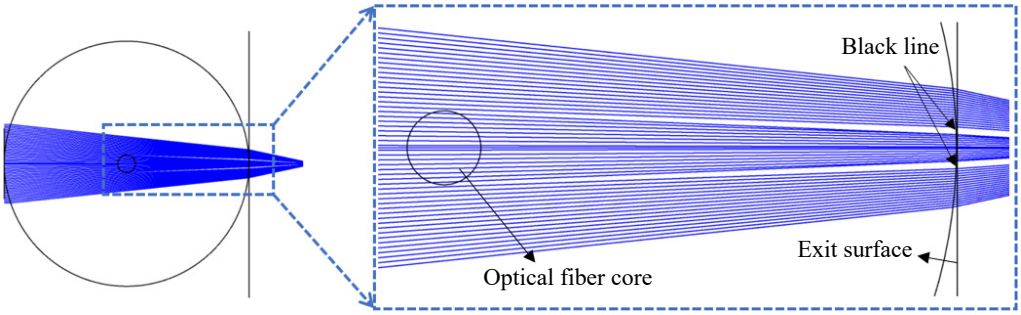

Fig. 1. Schematic diagram of a parallel light incident fiber.

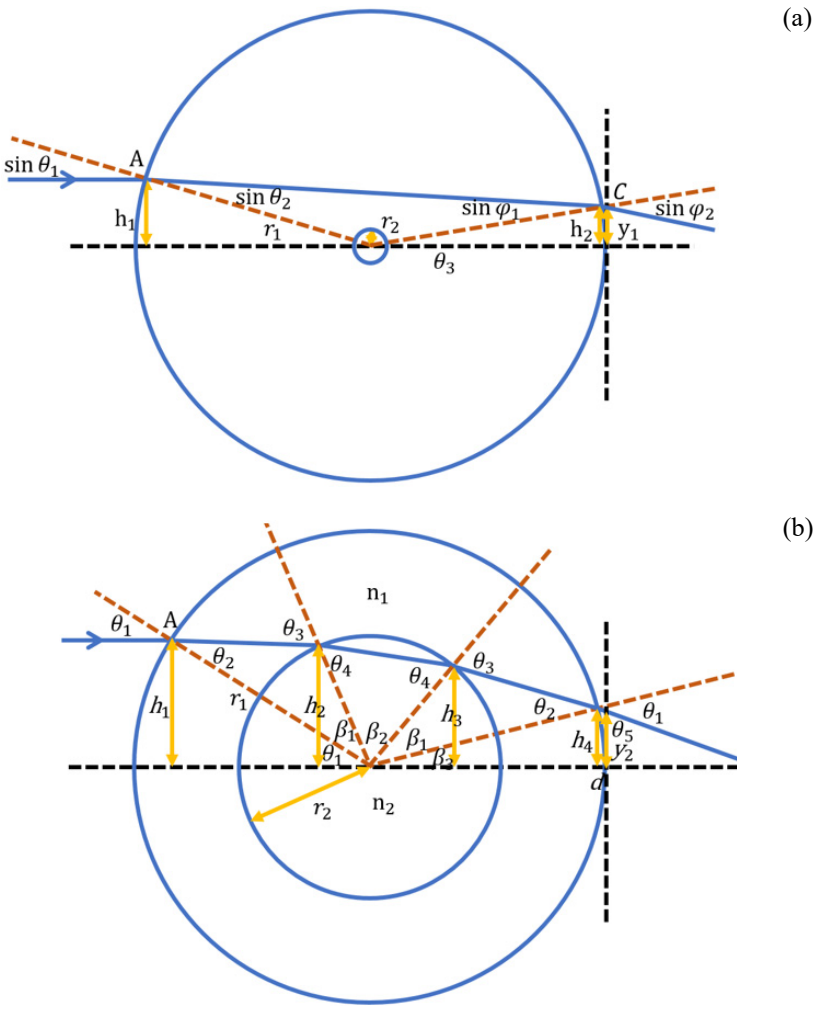

Fig. 2. (a) Schematic diagram of light propagation only in cladding in a single-core fiber. (b) The schematic diagram of light propagation through cladding and core in single-core fiber.

Figure 2(a) is a schematic diagram of light propagation in single-core fiber only in the cladding. The expression of the light height y_1 at the exit surface is calculated as follows:

$$y_1 = -r_1\left\{\sin\left[\arcsin\left(\frac{h_1}{r_1}\right)-2\arcsin\left(\frac{h_1}{r_1 n_2}\right)\right]+\tan\left[2\arcsin\left(\frac{h_1}{r_1}\right)-2\arcsin\left(\frac{h_1}{r_1 n_2}\right)\right]\right.$$
$$\left.-\tan\left[2\arcsin\left(\frac{h_1}{r_1}\right)-2\arcsin\left(\frac{h_1}{r_1 n_2}\right)\right]\cos\left[\arcsin\left(\frac{h_1}{r_1}\right)-2\arcsin\left(\frac{h_1}{r_1 n_2}\right)\right]\right\} \tag{1}$$

where, h_1 is the incident height of the light, r_1 is the cladding radius, r_2 is the core radius, n_1 is the refractive index of the fiber cladding, and n_2 is the refractive index of the fiber core. Figure 2(b) is schematic diagram of light propagation through the cladding and core in a single-core fiber. The calculation expression of the light height y_2 at the exit surface is:

$$y_2 = -r_1\sin\left[\arcsin\left(\frac{h_1}{r_1}\right)-2\arcsin\left(\frac{h_1}{n_1 r_1}\right)+2\arcsin\left(\frac{h_1}{n_1 r_2}\right)-2\arcsin\left(\frac{h_1}{n_2}\right)-r_2\right]$$
$$-r_1\cos\left[\arcsin\left(\frac{h_1}{r_1}\right)-2\arcsin\left(\frac{h_1}{n_1 r_1}\right)+2\arcsin\left(\frac{h_1}{n_1 r_2}\right)-2\arcsin\left(\frac{h_1}{n_2 r_2}\right)\right]$$
$$\times\tan\left[2\arcsin\left(\frac{h_1}{r_1}\right)-2\arcsin\left(\frac{h_1}{n_1 r_1}\right)+2\arcsin\left(\frac{h_1}{n_1 r_2}\right)-2\arcsin\left(\frac{h_1}{n_2 r_2}\right)\right] \tag{2}$$

According to the above two light height calculation formulas, the relationship between the light height of the exit surface of the optical fiber and the height of the incident light can be drawn. The single-mode light parameters are substituted into the formula to draw Fig. 3(a).

In Fig. 3(a), the upper and lower distance of the black dashed line is the black line width. By substituting different optical fiber parameters into the formula, the black line width corresponding to different types of optical fibers can be obtained, as shown in Fig. 3(b). The width of the fiber black line is closely related to the radius of the core and cladding. Under the condition that the core radius is constant, the width of the black line increases with the increase of the cladding radius. By amplifying the black line and using it as the basis for fiber splicing, the fiber position can be located more accurately.

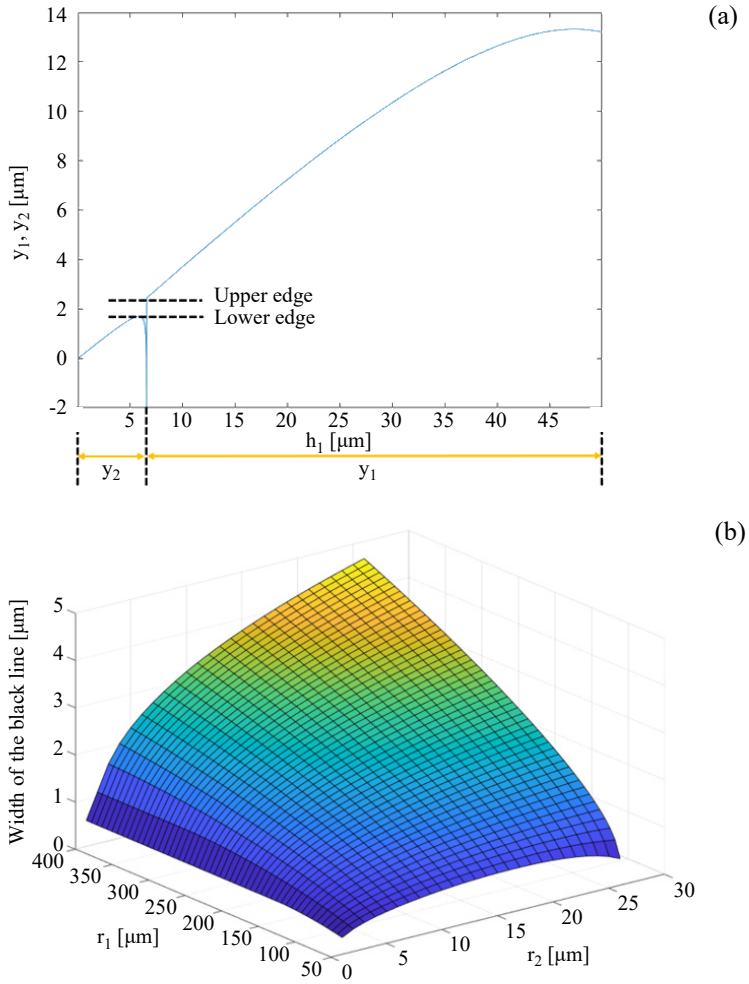

Fig. 3. (a) The relationship between the light height of the exit surface and the incident light height. (b) Diagram of the width of the black line corresponding to different cladding (r_1) and core (r_2) radius.

3. Optimum design

3.1. Design of high precision microscope objective for optical-fiber-fusion-splicing

In order to increase the width of the black line on the image plane as much as possible, it is necessary to reduce the influence of chromatic aberration on the width of the black line. The apochromatic mainly lies in the choice of lens glass material [10]. The microscope objective designed in this paper adopts a six-piece structure, and three glass materials are selected to meet the requirements of apochromatic. In the calculation of the initial structure of the lens, the whole system is divided into three groups, which are simplified into three lenses to solve the initial structure, as shown in Fig. 4.

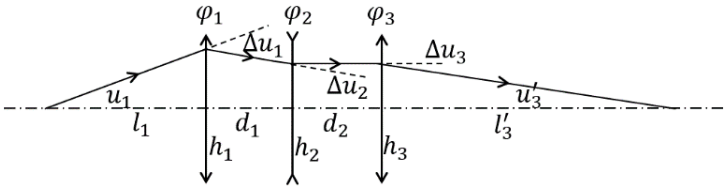

Fig. 4. Schematic diagram of lens optical focal length distribution.

The incident height of the light on each lens is different. The incident height of the light on the first lens is defined as h_1, the incident height of the light on the second lens is defined as h_2, and the incident height of the light on the first lens is defined as h_3. The light height is introduced into the light intensity, longitudinal aberration and secondary spectrum expression of the system:

$$\begin{cases} \varphi_1 + \dfrac{h_2}{h_1}\varphi_2 + \dfrac{h_3}{h_1}\varphi_3 = \Phi \\ \dfrac{\varphi_1}{v_1} + \left(\dfrac{h_2}{h_1}\right)^2 \dfrac{\varphi_2}{v_2} + \left(\dfrac{h_3}{h_1}\right)^2 \dfrac{\varphi_3}{v_3} = C_{\mathrm{I}} \\ \dfrac{\varphi_1}{v_1} P_1 + \left(\dfrac{h_2}{h_1}\right)^2 \dfrac{\varphi_2}{v_2} P_2 + \left(\dfrac{h_3}{h_1}\right)^2 \dfrac{\varphi_3}{v_3} P_3 = C_{\mathrm{II}} \end{cases} \tag{3}$$

The weighted focal power of the monolithic lens is defined as φ'_i, the weighted Abbe number is v'_i, and the weighted relative partial dispersion is P'_i. Substituting the weighted expression of the single lens into the result for analysis, the separated three -lens focal power distribution expression can be obtained:

$$\begin{cases} \varphi'_1 = \Phi \dfrac{v'_1(P_3 - P_2)}{\Delta'} \\ \varphi'_2 = \Phi \dfrac{v'_2(P_1 - P_3)}{\Delta'} \\ \varphi'_3 = \Phi \dfrac{v'_3(P_2 - P_1)}{\Delta'} \end{cases} \quad \begin{cases} \varphi'_i = \varphi_i \dfrac{h_i}{h_1} \\ \dfrac{1}{v'_i} = \dfrac{1}{v_i}\dfrac{h_i}{h_1} \\ \dfrac{P'_i}{v'_i} = \dfrac{P_i}{v_i}\dfrac{h_i}{h_1} \end{cases}, \quad \Delta' = \begin{vmatrix} P_1 & v'_1 & 1 \\ P_2 & v'_2 & 1 \\ P_3 & v'_3 & 1 \end{vmatrix} \tag{4}$$

It can be seen from the Eq. (4) that the distribution expression of the focal power of the separated three lenses is meaningful only if the denominator is not 0, that is, $\Delta' \neq 0$. From the perspective of subsequent aberration correction, the larger the value of Δ' is, the smaller the focal power of each lens is. After satisfying the condition of apochromatic aberration, it is more conducive to correcting the remaining aberrations.

The microscope objective designed in this paper can be divided into front group, relay group and latter group. Because the arc discharge during fiber fusion will cause high temperature, and the lens distance is too close to contaminate debris, the whole system adopts + − + focal power distribution to increase the working distance [11]. As shown in Fig. 4, the focal power of the three components is φ_1, φ_2, and φ_3, respectively. The focal power of the front group and the latter group is positive, and the focal power of the relay group is negative. The incident aperture angles of the front group, the relay group and the latter group are u_1, u_2, and u_3, respectively. The exit aperture angles are u_1', u_2', and u_3', respectively. The deflection angles of the light on each group are Δu_1, Δu_2, and Δu_3, respectively. The object distance is l_2. The distance between the front group and the relay group is d_1, the distance between the relay group and the latter group is d_2, and the image distance is l_3'.

T a b l e 1. Specifications of optical fiber microscope objective.

Parameters	Value
Working waveband	460–660 nm
Numerical aperture	0.18
Magnification	5.5

The proportion of light deflection angle of each group is set below, with the front group taking the main deflection angle and having a larger focal power. The light deflection angle of the relay group and the latter group is smaller and bears a smaller focal power, and the combination of the negative focal power of the relay group and the positive focal power of the latter group is used to correct the spherical aberration and longitudinal aberration of the system, and the ratio of the light deflection angle of each group is as follows:

$$\Delta u_1 : \Delta u_2 : \Delta u_3 = 1 : (-0.21) : 0.21 \tag{5}$$

according to the numerical aperture of the microscope objective and the proportion of the light deflection angle of each component. The deflection angle range borne by the former group is 12–15°, the deflection angle borne by the relay group is 4–7°, and the deflection angle borne by the latter group is 3–6°. Based on the above light incident angle and multi-light group combination calculation formula, the focal power distribution of the three light groups φ_1, φ_2, and φ_3 can be obtained. The focal power of the former group $\varphi_1 = 0.054$ mm^{-1}, the relay group $\varphi_2 = 0.007$ mm^{-1}, and the latter group $\varphi_3 = 0.004$ mm^{-1} were calculated.

3.2. Results of non-sequential simulation experiments

The microscope objective designed in this paper mainly magnifies the black line. The longitudinal aberration is identified as the primary factor affecting the width of the black line. The balance of the longitudinal aberration is a key consideration when optimizing the design. The longitudinal aberration reacts to the different wavelengths

at the axial convergence point position, and reducing the longitudinal aberration of the system can effectively increase the width of the black line. After balancing the longitudinal aberration, correcting the secondary spectrum at the position of the aperture corresponding to the black line can further increase the black line width. The correction of the secondary spectrum is related to the Abbe number and partial dispersion of the glass material, and according to the above derivation of the apochromatic of the system, the appropriate glass material is selected in the glass library for optimization.

In order to be closer to the real situation, it is necessary to perform simulation experiments for verification. As shown in Fig. 5, from left to right, there are light source, optical fiber, microscope objective and detector. The parallel light emitted from the light source is refracted by the core of the optical fiber cladding, and the exit angle changes to a divergent beam, which is received by the microscope objective through the core and part of the cladding fiber, and imaged on the detector after amplification. Figure 6(a) is the image received on the detector. It can be seen from the figure that

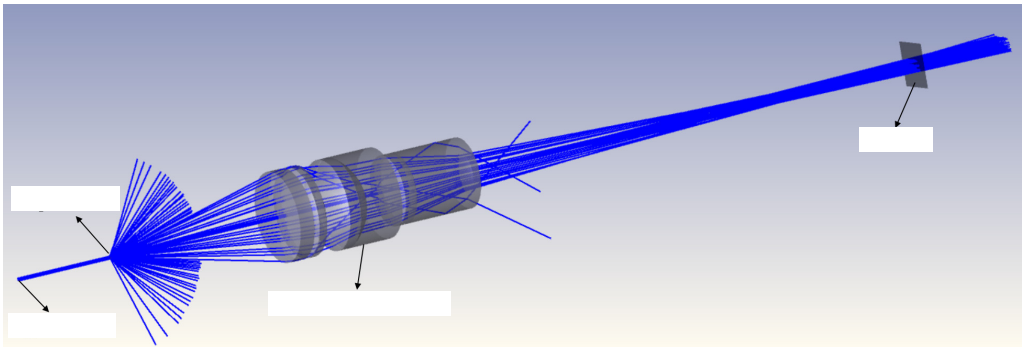

Fig. 5. Schematic of non-sequential optical fiber fusion splicing microscope objective simulation.

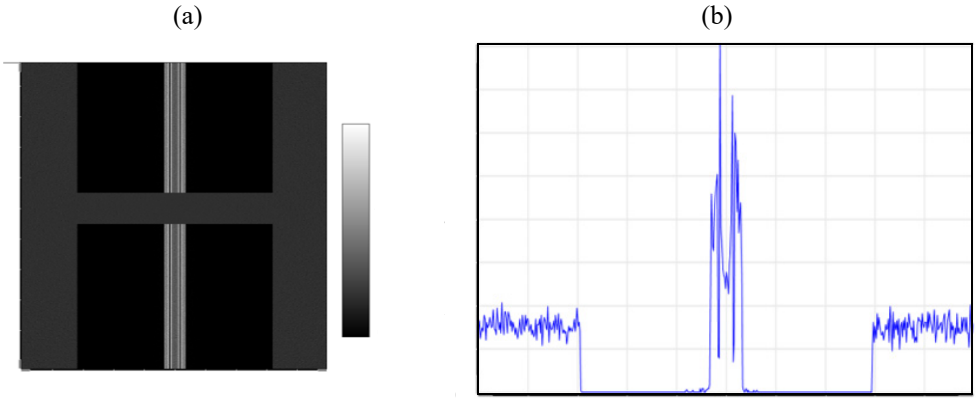

Fig. 6. Detector received image. (a) Gray-scale image received by the detector. (b) Cross-section of light intensity distribution.

the edge of the fiber image is clear, and there is an obvious black line between the cladding and the core, which can be used as the alignment basis for fiber splicing. From the light intensity distribution cross-sectional Fig. 6(b), it can also be seen that the light intensity inside the fiber is strong, and there are two symmetrically distributed very steep peaks and valleys, corresponding to the black line at the boundary between the fiber cladding and the fiber core. The contrast characteristics are very obvious, which is suitable for the basis of fiber alignment.

4. Experimental verification and image feature extraction

4.1. Experimental system setup

After completing the optical structure design of the lens, a suitable mechanical structure is designed to fix the optical components. In this paper, the pressure ring, the spacer ring and the lens barrel are designed. The combined optical-mechanical structure is shown in Fig. 7. After the processing of the microscope objective is completed, an experimental device is built for verification.

The experimental setup is shown in Fig. 8. After the beam emitted from the light source is collimated by the light source collimating mirror, the collimated beam is in-

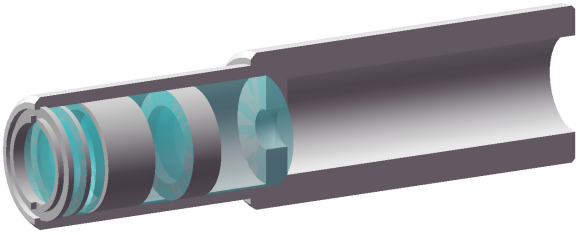

Fig. 7. Assembly diagram of optical fiber fusion splicing microscope objective.

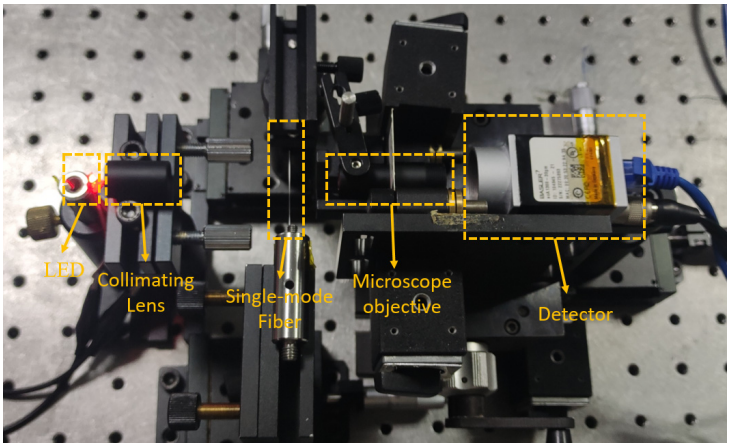

Fig. 8. The schematic diagram of optical fiber microscope objective experimental device.

cident on the fiber from the side. After refraction by the fiber core and cladding, it enters the designed microscope objective and is finally imaged on the detector. In this paper, LED is selected as the light source of the system. The collimating lens is used to collimate the light source, and the collimation of the light is controlled within 5%.

From the images taken in the experiment, it can be seen that the designed optical fiber side alignment microscopic imaging system clearly observes the black line at the boundary between the fiber core and the cladding, which can be used as an important feature of fiber alignment. Improve the accuracy of fiber alignment to meet the design requirements.

4.2. Black line feature extraction of optical fiber

After obtaining the fiber image, the image is processed to obtain the characteristics of the fiber. Firstly, for the input fiber image, the gradient of the image is calculated by Sobel operator, and the gradient intensity and direction information of each pixel in the image are obtained [12, 13]. Then, in the non-maximum suppression stage, the image after gradient calculation can be compared with the image after non-maximum suppression processing, and the pixel with the largest local gradient can be retained to suppress the gradient response in other directions [14, 15]. Finally, the edge lines finally determined by the Canny algorithm are displayed. Figure 9 shows images with the highest thresholds of 0.02, 0.1and 0.3, respectively. Attempting a lower threshold will lead to too many edges, as shown in Fig. 9(a), affecting the accuracy of the edges and adversely affecting the subsequent selection of edge features. If the threshold is too high, part of the edge will be lost, resulting in a lack of image information.

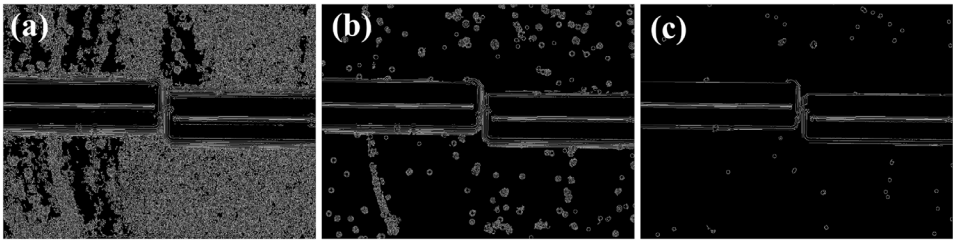

Fig. 9. Optical fiber image edge. Threshold of (a) 0.02, (b) 0.1, and (c) 0.3.

The purpose of feature extraction is to obtain the relative distance between the horizontal and vertical directions of the optical fiber, so it is divided into two parts. The first is the horizontal position offset of the two optical fibers, which is characterized by the intensity change of the optical fiber image on the cross-section. Combined with the edges screened by Canny in the above, the pixel position with the largest pixel gradient is obtained. This pixel position is the point where the light intensity changes most drastically, that is the end position of the fiber. After calculation, the horizontal offset of the optical fiber in the diagram is 33.6 μm.

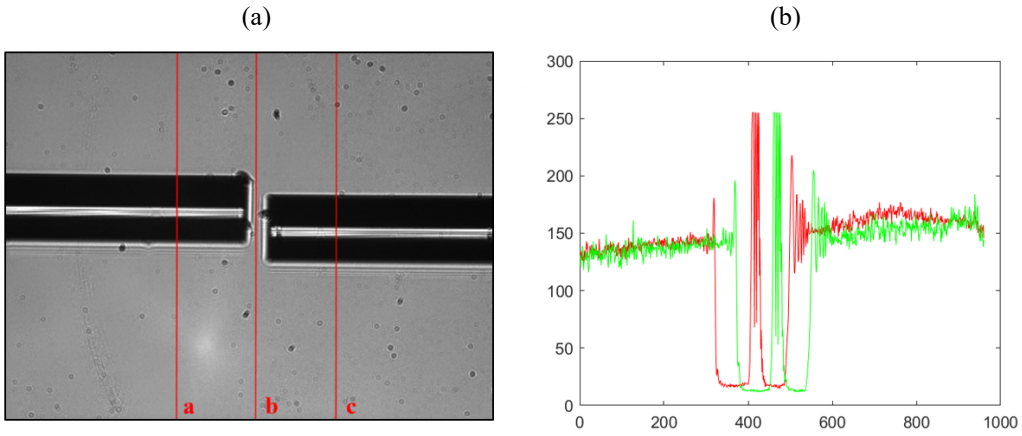

Fig. 10. (a) Schematic column cross-section of the fiber image. (b) Light intensity profiles of the left and right fibers.

The feature extraction of the vertical position of the fiber is relatively complex, and the selection of the key features is done in the light intensity map of the column section in the fiber image, as shown in Fig. 10(a). The design focus of the microscope objective mentioned above is the black line between the cladding and the fiber core. The black line has very significant features. In the feature extraction step of image processing, the focus is on identifying and exploiting the features of the black line, and finally the vertical offset of the two fibers is obtained.

The light intensity cross-sections of the two fibers corresponding to *a* and *c* in Fig. 10(a) are placed together for comparison. As shown in Fig. 10(b), the red light intensity curve in the figure represents the fiber on the left, and the green light intensity curve represents the fiber on the right. The overall trend of the light intensity curves of the two fibers is approximately the same, but there is a shift in the figure. This shift corresponds to the difference in the vertical position of the two fibers.

The process of finding the position of the black line is simply to iterate through each column of the image, find the minimum points in each row, and determine the position and size of all the minimum points. Then, by using the characteristics of the black line, the light intensity of the black line is in a special interval, which is smaller than the external light intensity of the transparent fiber and weaker than the energy of the opaque part of the inner cladding of the fiber, so that a large number of irrelevant minimum points are excluded. Further, the black line is located in the interval with strong light intensity inside the fiber. The interval intensity weighted average is used to screen the weakest energy interval of the cladding and the strongest energy interval of the fiber core to determine the correct interval position of the black line. In this way, only the minimum point positions corresponding to the two black lines are left, as shown in Fig. 11, and the blue circle in the figure is the excluded minimum point position, and the point marked by the red circle is the black line position we need. Fur-

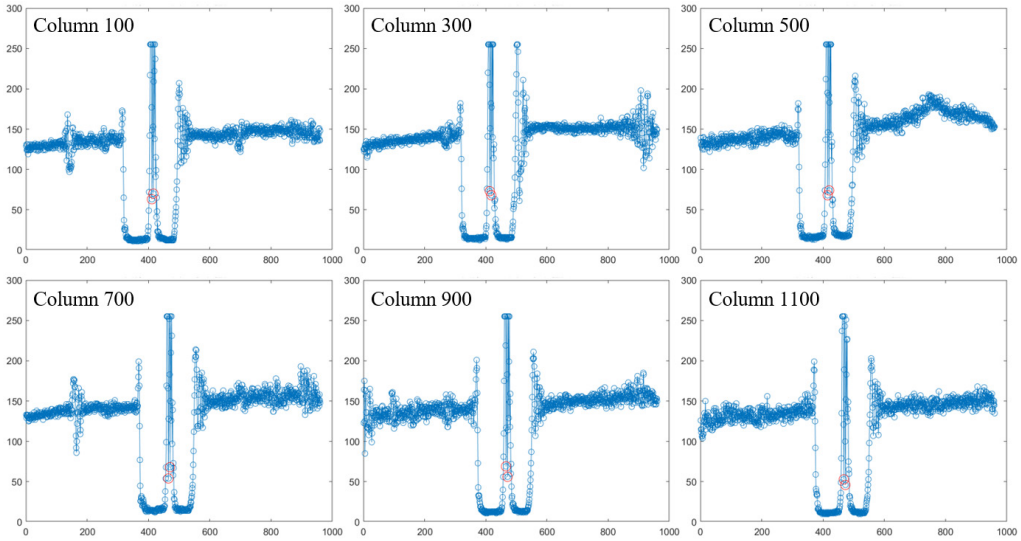

Fig. 11. Minimum value point images on different columns of the optical fiber image.

thermore, the edge extracted by Canny operator can further reduce the interval of the minimum point and further reduce the computational complexity of the program.

Iterate the light intensity map of the column section with the optical fiber, find out the black line position corresponding to each column section, classify the black line points of the left and right two optical fibers, respectively, and classify the black lines above and below each optical fiber. In this way, four sets of data on the position of different black lines are obtained, and each set of data is integrated. The position of the black line obtained by fitting is marked on the map, as shown in Fig. 12. By comparing the vertical positions of the left and right fibers, the vertical distance required for fiber alignment is obtained, and the vertical offset is calculated to be 36.4 μm.

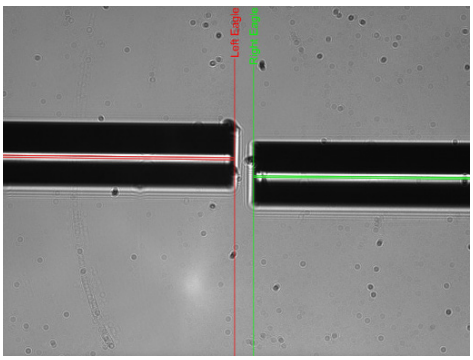

Fig. 12. Image of optical fiber end positions and black line positions.

5. Conclusion

In this paper, the distribution law of the parallel light side irradiation after entering the fiber is studied, and an alignment method based on the black line at the interface between the fiber core and cladding is proposed. According to the imaging characteristics of the black line, an optical fiber microscope head is designed to enhance the details of the black line. Based on the achromatic theory, the initial structure of the microscope objective is deduced. The lens design theory is verified through a simulation imaging experiment. And the experimental device is built to capture the optical fiber image through the microscope objective. Image preprocessing, edge detection, and feature extraction are performed on the captured image to obtain the image features of the optical fiber. The distance between the end surfaces of the two fibers corresponds to the horizontal offset of the fiber, and the black line corresponds to the vertical offset of the fiber. The position of the end surface is determined by the edge detection algorithm, and the position of the black line is obtained by the characteristics of the ordinate light intensity curve of the optical fiber image. Finally, the horizontal and vertical offsets of the optical fiber are obtained. In this paper, the lens design theory and feature recognition algorithms are comprehensively considered to improve the accuracy of optical fiber alignment from two aspects, and ultimately to achieve high quality optical fiber splicing.

Acknowledgment
This work was supported by the National Natural Science Foundation of China (61405134 and 61340007); National Defense Basic Scientific Research (JCKY2018414C013); Natural Science Foundation of Jiangsu Province (BK20161512); Priority Academic Program Development of Jiangsu Higher Education Institutions (PAPD).

References

[1] Habib M.S., Antonio-Lopez J.E., Markos C., Schülzgen A., Amezcua-Correa R., *Single-mode low loss hollow-core anti-resonant fiber designs*, Optics Express **27**(4), 2019: 3824-3836. https://doi.org/10.1364/OE.27.003824

[2] Xiao L., Jin W., Demokan M., *Fusion splicing small-core photonic crystal fibers and single-mode fibers by repeated arc discharges*, Optics Letters **32**(2), 2007: 115-117. https://doi.org/10.1364/OL.32.000115

[3] Ding W., Wang Y.Y., Gao S.F., Wang M.L., Wang P., *Recent progress in low-loss hollow-core anti -resonant fibers and their applications*, IEEE Journal of Selected Topics in Quantum Electronics **26**(4), 2020: 4400312. https://doi.org/10.1109/JSTQE.2019.2957445

[4] Yang S., Yuan L., *Connecting technologies for coaxial dual core optical fiber*, Journal of Lightwave Technology **38**(23), 2020: 6629-6634. https://doi.org/10.1109/JLT.2020.3014652

[5] Hu L.W., Yuan C.W., *Modeling and analysis of the fusion strength of single-mode optical fiber in the high altitude environment*, Optical Materials Express **12**(8), 2022: 2995-3014. https://doi.org/10.1364/OME.463907

[6] Zhang Z., Li R., Wang C., Zhou M., Liu Y., Pang Y., *Fusion splicing of hollow-core to standard single-mode fibers using a gradient-index bridge fiber*, Journal of Optical Technology **90**(1), 2023: 42-45. https://doi.org/10.1364/JOT.90.000042

[7] WANG Y., BARTELT H., BRUECKNER S., KOBELKE J., ROTHHARDT M., MÖRL K., ECKE W., WILLSCH R., *Splicing Ge-doped photonic crystal fibers using commercial fusion splicer with default discharge parameters*, Optics Express **16**(10), 2008: 7258-7263. https://doi.org/10.1364/OE.16.007258

[8] DEBORD B., AMSANPALLY A., CHAFER M., BAZ A., MAUREL M., BLONDY J. M., HUGONNOT E., SCOL F., VINCETTI L., GÉRÔME F., *Ultralow transmission loss in inhibited-coupling guiding hollow fibers*, Optica **4**(2), 2017: 209-217. https://doi.org/10.1364/OPTICA.4.000209

[9] WANG Z.F., BELARDI W., YU F., WADSWORTH W.J., KNIGHT J.C., *Efficient diode-pumped mid-infrared emission from acetylene-filled hollow-core fiber*, Optics Express **22**(18), 2014: 21872-21878. https://doi.org/10.1364/OE.22.021872

[10] ZHANG K., LI J., SUN S., WANG J., YU S., *Optical system design of double-sided telecentric microscope with high numerical aperture and long working distance*, Optics Express **31**(14), 2023: 23518-23532. https://doi.org/10.1364/OE.496322

[11] MIKŠ A., NOVÁK J., *Method of calculation of initial design parameters of microscope objective lenses with a long working distance*, Applied Optics **61**(12), 2022: 3288-3296. https://doi.org/10.1364/AO.455543

[12] WU G., SONG Z., HAO M., YIN L., *Edge detection in single multimode fiber imaging based on deep learning*, Optics Express **30**(17), 2022: 30718-30726. https://doi.org/10.1364/OE.464492

[13] HEBERT T.J., MALAGRE D., *Optimization approach to edge detection*, Journal of the Optical Society of America A **11**(1), 1994: 80-88. https://doi.org/10.1364/JOSAA.11.000080

[14] PENG X., KONG L., *Defect extraction method for additive manufactured parts with improved learning-based image super-resolution and the Canny algorithm*, Applied Optics **61**(28), 2022: 8500-8507. https://doi.org/10.1364/AO.467923

[15] BEVILACQUA M., ROUMY A., GUILLEMOT C., MOREL M.L.A., *Single-image super-resolution via linear mapping of interpolated self-examples*, IEEE Transactions on Image Processing **23**(10), 2014: 5334-5347. https://doi.org/10.1109/TIP.2014.2364116

Received June 13, 2024